Nonlinear Phenomena in Complex Systems, vol. **25**, no. 1 (2022), pp. 21 - 40

Topologically Tuned Obliquity of Klein-Tunnelling Charged Currents Through Graphene Electrostatically-Confined $p-n$ Junctions

Halina Grushevskaya* and George Krylov†
Physics Department, Belarusian State University,
4 Nezalezhnasti Ave., 220030 Minsk, BELARUS
(Received 17 January, 2021)

Problem of control over Klein-tunnelling states from electrostatically-confined graphene $p-n$ junctions has been discussed. The lack of quasi-bound states, being the states with a finite life time, in a pseudo-Dirac-fermion model for the graphene quantum dot (GQD) is theoretically predicted as inapplicability of the so-called "resonance condition" leading to an inconsistent linear system corresponding to matching conditions. Within a pseudo-Dirac-Weyl fermion model GQD, the graphene charge carriers are topologically nontrivial and can be confined by a staircase-type potential due to competition between Zak curvature and centrifugal-force actions. The predicted topological effects elucidate experimentally observed resonances created by electron beam and laser pulse in crystalline arrays of single-walled carbon nanotubes as the Klein-tunnelling resonant states in the $p-n$ graphene junctions. We present a robust approach to fabricate stable graphene $p-n$ junctions by fine-tuning the topological effects.

PACS numbers: 73.63.Kv, 73.23.Ab, 73.43.Cd, 81.05.Uw, 73.63.Kv
Keywords: graphene, quantum dot, pseudo-Dirac fermion, Klein tunneling, quasi-bound state
DOI: https://doi.org/10.33581/1561-4085-2022-25-1-21-40

1. Introduction

Since more than twenty years of its experimental observation, graphene still attracts a lot of attention and attempts to use it as a platform to develop super-high speed electronic devices and communications. The huge Fermi velocity value (v_F of about 10^6 m/s) for two-dimensional (2D) graphene charge carriers is owing to their masslessness but the high carrier mobility disappears when doping even reasonably to form a predefined band gap needed for the transistor-like behavior. A way of electric-current operation on the graphene is to utilize graphene quantum dots without physical termination as the graphene-based devices for the future electronics, sensors, and quantum information technologies. The most promising ones are so-called electrostatically confined circular GQDs or graphene $p-n$ ($n-p$) junctions because of bipolarity retaining [1–4]. The $p-n$ ($n-p$) junctions are produced by an electrical field applied to a graphene patch when $n(p)$ doping a bulk monolayer graphene. The electrical field created by a scanning tunnelling microscope (STM) tip polarizes some nanometer-sized patch of the graphene plane so that touchings between conical conducting and valent bands shift producing an energy gap in the band structure. Brillouin-zone valleys K and K' called as Dirac points correspond to the energy band touchings. A charge leakage from the junctions happens due to Klein scattering [5] which always exists for the graphene massless charge carriers. As a result the defects disappear in time. To utilize the p-n (n-p) junction one needs to tune the junction parameters in such a way that the charge density redistribution due the Klein tunnelling is very small. The charge carriers oblique by a radial

*E-mail: grushevskaja@bsu.by
†E-mail: krylov@bsu.by

field are precluded from the Klein tunnelling. The tuning is in giving an obliquity for the graphene charge carrier motion so that the graphene-charge carriers skirt round the obstacles and a number of holes (electrons) normally incident on a potential barrier (well) is negligible.

Two variants of such a tuning are known. First, the rotational symmetry of the graphene circular patch (obstacle) which is created by a STM tip voltage pulse resulting in the shift of the Dirac-point energy originates a centrifugal force $f \propto \frac{m}{R}$ along the circular-obstacle boundary (see [6] and references therein). Here $m = l + \frac{1}{2}$ is an integer, $l = \pm\frac{1}{2}, \pm\frac{3}{2}, \ldots$ is the angular momentum quantum number, R, $R \ll 1$ is the quantum-dot radius. The Klein tunnelling resonances being obliqued the pseudo-Dirac fermions which constructively interfere subsequently are similar to whispering-gallery modes. Second, a Coulomb potential of a double STM tip produces the obliquity. In this case, the GQD is similar to an artificial atom with a huge number of electrons, as the effective electric charge of Coulomb potential or the Coulomb coupling $\beta = (Z/\epsilon_G)\alpha c/v_F$, which confines charge carriers in the tip-induced junction, takes on values typical for a supercritical regime of ultra-heavy atoms. In this regime the electronic orbitals, starting with 1s state sink into Dirac continuum until an atomic number Z is reduced to the critical value [7, 8]. Here Z is a local unscreened charge, c is the speed of light, ϵ_G is the effective dielectric constant of bulk graphene, $\epsilon_G \approx 5$, $\alpha \sim 1/137$ is the fine structure constant [9]. The electron moving down on levels of the ultra-heavy nuclei causes an atomic collapse because the coupling holding the charge carrier vanishes. The last one continues its motion under the action of the centrifugal force. The tip-induced junction states are called as atomic collapse states.

Assumptions on the nature of the electrostatic geometric confinement are controversial. In the first case, since the force $f \propto \frac{m}{R}$ has a symmetrical origin it should be linked with a GQD topology. However, the geometrical centrifugal force acting on the GQDs with sphere topology holding a non-zero curvature destroys Bohr-atom-like orbitals formed on resonant trajectories (with an integer number of wave periods on the trajectory) and, oppositely, for the GQDs of toroidal type the interference is possible due to the lack of the geometrical curvature [10]. Besides, for both the whispering-gallery modes and atomic collapse, the wave function of the graphene charge carriers enveloping the geometric obstacle acquires additionally a Berry phase (more precisely, Zak phase). For example, a plane wave function $\propto \exp(-i\vec{k} \cdot \vec{r})$ of the pseudo-Dirac graphene fermion changes to $\propto \exp(i\vec{k} \cdot \vec{r})$ because the phase of the wave function changes on π. It signifies that the chiral electron (hole) becomes a chiral hole (electron). But, such a transformation is prohibited by the chirality conservation law.

In [11] to study topology effects the $p - n$ and $(n - p)$ graphene junctions were fabricated by the tip voltage pulsing technique, locating (placing) a graphene monolayer over another graphene monolayer when Bernal stacking. The experimental data indicate the change of the Berry phase on π (flip or change of the sign of the Berry curvature) by changing the type of GQD doping on an inverse one (a $n - p$ junction is created instead of the $p - n$ junction and vise versa). It signifies that a violation of the chirality is forbidden (electrons (holes) can not change direction of momentum) and the chirality conservation law is exhibited through a GQD rotational symmetry broken to $\mathcal{C}_3$. Contrary to this, a nonrelativistic tight-binding hamiltonian of the model bilayer graphene (BLG) predicts that a trigonal warping of the graphene band structure remains a hexagonal symmetry of the GQD model and, correspondingly, the circularly symmetric form of the GQD states [3, 12, 13]. because the three flat regions hosted by the BLG band structure can not produce such topologically nontrivial obstacles.

Thus, the presence of a centrifugal force does not guarantee that the waves of the oblique charge carriers constructively interfere. Moreover, the chirality which prevents constructive interference,

casts doubt on an existence of the whispering-gallery modes and atomic collapse states.

So, creating well-controlled $p-n$ $(n-p)$ graphene junctions turned out to be extremely challenging. One needs more investigations to understand the origin of the quantum interference process in the graphene quantum dots.

Most theoretical investigations predicted circularly symmetric GQD states within a pseudo-Dirac fermion graphene hamiltonian with a radial step [1] (see also other approaches in [14] and references therein) or multistep [12] (radial parabolic potential) potentials. Specific feature of quantum problems for the 2D massless pseudo-Dirac equation with the circular symmetric finite-height potential barrier is the absence of bound eigenstates. This is stipulated by the fact that solutions of the Dirac radial equation in a region with a flat potential are linear combination of the Bessel functions which asymptotically look like slowly decreasing sine and cosine and therefore the eigenstates are non-normalizable and correspond to unbound particles.

In [1] it has been stated the existence of the quasi-bound eigenstates for this problem, complex-energies imaginary parts of which correspond to a level's decay time. The eigenstates were chosen from some sort of a "spectral condition" arisen in consideration. In [1] and [3] the deduction of this condition were slightly different, in the first one it has been derived for admissible system eigenstates, in the second paper the condition was deduced for the scattering problem. In subsequent publications there were made a lot of experimental works to be interpreted by these theoretical predictions [3, 4, 14–16]. However, the experimental validation of these predictions is lacking.

In our paper we will prove with all detail in both cases the existence of such type of quasi-bound states is impossible. The theoretical prediction will be experimentally verified by experiencing with electron-beam and Raman light scattering on arrays of single-walled carbon nanotubes (SWCNTs) as arrays of rolled graphene monolayers. The arrays are crystalline SWCNT monolayers fabricated by a Langmuir–Blodgett (LB) technique.

The current paper aims to offer experimental evidences and theoretical predictions that a circular motion of graphene charge carriers obliqued by radially symmetric electrical fields creating the graphene structural defects is precluded due to their chirality (the pseudo-spin conservation law) and that the electrostatic geometric confinement in a monolayer graphene is unstable in the radial step potentials. We present also conclusive evidences that competition between the centrifugal force and force associated with the topological charge (the vorticity of the charge-carrier density) confines the graphene charge carriers in the $p-n$ $(n-p)$ junctions.

2. Materials and methods

2.1. Materials

Few-wall carbon nanotubes (CNT) purchased from Fibermax (Greece) were utilized. The CNTs with smaller diameter below $2-2.5$ nm and length of $\sim 5-10$ μm were produced by the method of chemical vapor deposition (CVD-method). The raw CNTs are covalently modified by carboxyl groups and non-covalently functionalized by stearic acid molecules.

Salts $Fe(NO_3)_3 \cdot 9H_2O$, $Ce_2(SO_4)_3$ (Sigma, USA), hydrochloric acid, deionized water with resistivity of 18.2 $M\Omega$·cm were used to preparate subphases. An amphiphilic oligomer of thiophene-pyrrole derivatives with chemically bounded hydrophobic 16-link hydrocarbon chain R: 3-hexadecyl-2,5-di(2-thienyl)-1H-pyrrole (H-DTP, H-dithienylpyrrole), chemical structure of which is shown in Fig. 1a was utilized to synthesize a nanocyclic compound (Fe(II)DTP) of the dithienylpyrrole with hight-spin divalent Fe(II) decorating carbon nanotubes [17]. The Fe(II)DTP films are fabricated by the LB technique [18]. The complex of Fe(II)DTP is presented in Inset to

Fig. 2.

2.2. Methods

2.2.1. Structural and diffraction methods

Electron microscopy.

Scanning electron microscopy (SEM) images were taken on LEO 1455 VP (Carl Zeiss, Gernamy) JEM-100CX. The accelerating voltage was 20 kV. Signals of reflected and secondary electrons were detected simultaneously. In order to determine crystallographic characteristics of crystallites the diffraction appliance to the scanning electron microscope – HKL EBSD Premium System Channel 5 was used (Oxford Instruments, England). To obtain a reflected electron (electron backscatter) diffraction (RED) patterns, a sample was placed on a special table, having a tilt angle to the horizontal of about 70 degrees. Electron probe was directed to the point of interest on a sample surface: elastic scattering of the incident beam causes the electrons to be deviated from the point directly below the sample surface and the bump on crystal planes from all sides. In cases when a Bragg diffraction condition is satisfied for the planes formed by atoms of the crystal lattice, two conical beams of diffracted electrons are formed for each family of crystal planes. These cones of electrons can be visualized by placing on their way a phosphorescent screen and after it a highly-sensitive camera for observation (digital CCD camera). In places where the cone-shaped electron beams intersect with the phosphorescent screen, they appear as thin bands called Kikuchi bands (see [19] and references therein). Each of these bands corresponds to a specific group of the crystal planes. The resulting RED pattern consists of many Kikuchi's bands. With the help of the Flamenko software the position of each Kikuchi's band was automatically determined, comparison with theoretical data and the conclusion on corresponding crystalline phase were performed as well as a three-dimensional crystallographic orientation was calculated. To record the RED patterns the samples were previously deposited on amorphic SiO_2 supports.

Microdiffraction patterns and transmission electron microscopic (TEM) images were obtained by means of transmission electron microscope JEM-100CX (JEOL, Japan) at accelerating voltage of 100 kV. The samples were previously deposited on a copper grid with a formvar polymer coating or on nanoporous anodic alumina (AOA) membranes from the direction of the barrier AOA layer the pore diameter is of 19 nm.

Atomic-force microscopy.

AFM experiments were performed at room temperature in ambient air on a Nanoscope Solver P47 Pro (NT-MDT Company, Zelenograd). Silicon tips (NCH, NanoWorld Ltd Co.) with a spring constant of 2.5–10.0 N m^{-1} (Resonance frequency: 115–190 kHz) were employed. Topographic images were recorded in a non-contact mode (tapping) with a tip velocity of 2.5 μm s^{-1}, a scan rate of 0.5 Hz and a scan angle of 90°. When scanning the sample an amplitude change was recorded, that has been written into computer RAM (random access memory) as an image of the surface relief. Simultaneously when scanning the sample at each point a change of a phase of cantilever oscillations is recorded, and the change is written as a distribution of phase contrast. The samples for AFM imaging were previously deposited on graphite fresh cleavages.

2.2.2. CNT-monolayer fabrication

Ultra-thin 2- or 3-monolayer LB-films consisting of the carboxylated SWCNTs decorated or non-decorated by the nanocyclic complexes of high-spin octahedral Fe(II) with the ligands of the dithionylpyrrole series are fabricated in the following way. The SWCNT bilayers of the Y-type are formed by the LB-nanotechnique of depositing two Langmuir crystalline SWCNT monolayers on AOA membranes, graphite fresh cleavages, Si supports, and copper grids with formvar polymer

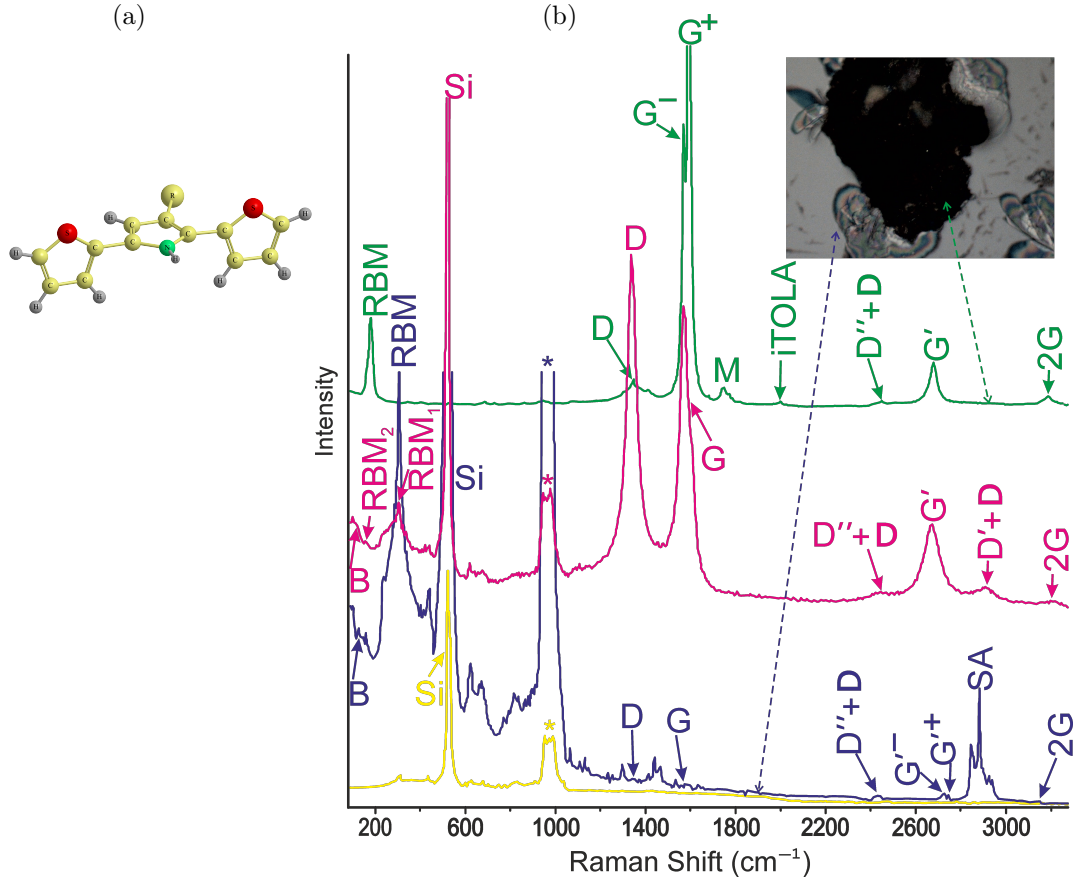

FIG. 1. (a) Chemical structure of H-dithienylpyrrole molecule. (b) Raman spectra of original few-walled CNTs (magenta curve), hydrophobic stearic-acid micelles with metallic (blue curve) and semiconducting (green curve) SWCNTs, and Si support (yellow curve). Images of the micellar samples are inset on the right side of the figure. Symbols "Si", "SA", and "*" designate the vibrational modes of Si (at 519.57 cm^{-1}), stearic acid, and the laser peak (at the frequency 980 cm^{-1}), respectively. The Si/SiO_2 spectrum was recorded at 24 K, all other spectra were recorded at RT. Inset: a confocal microscopy image of a dark-colored conglomerate of micellar semiconducting SWCNTs surrounded by bright rainbow-colored associates of micellar metallic SWCNTs.

coating.

Preliminary, the inverse micelles of stearic acid with the few-walled CNTs inside were obtained by mixing the stearic acid and CNTs in hexane by the ultrasound treatment, and then the SWCNT crystalline monolayer was formed by compressing a Langmuir monolayer of the micellar SWCNTs on the surface of deionized water.

The AOA and Si supports were covered by the five crystalline Fe(II)DTP monolayers; the cooper grids were covered by three or five crystalline Fe(II)DTP monolayers. The three-monolayer SWCNT LB-film of the Y-type was deposited on the copper grid with the formvar polymer coating only.

2.2.3. Raman spectroscopy

Spectral studies in visible range were carried out using a confocal micro-Raman spectrometer Nanofinder HE ("LOTIS-TII", Tokyo, Japan–Belarus) on lasers operating at wavelengths of 355 (external laser), 473 (DPSS laser), and 532 (DPSS laser) nm with power in the range from 0.0001 to

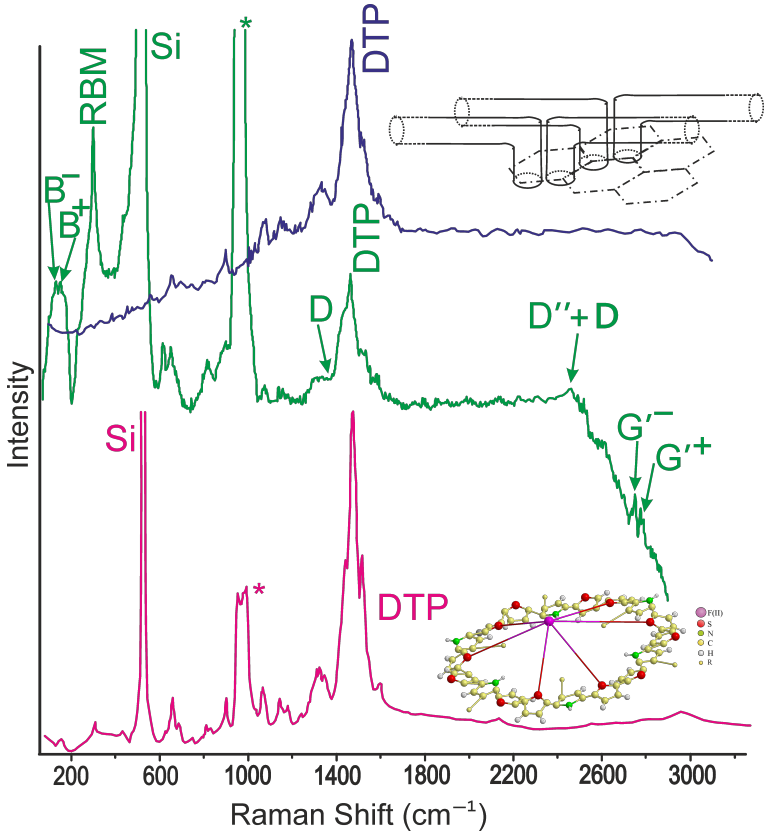

FIG. 2. Raman spectra of 2-monolayer LB-CNT-films deposited on Si (green curve) and 10-nm-porous AOA (blue curve). The CNT LB-films are deposited on the 5 LB-monolayers fabricated from the nanocyclic complexes Fe(II)DTP. A Raman spectrum of the Fe(II)DTP LB-film is shown in the figure (magenta curve). Inset: (up) cartoon of the CNT-monolayer structure and (down) a chemical formula of Fe(II)DTP.

20 mW. The spectra were recorded in the back-scattering geometry under a × 50 objective at room (RT) and low (24 K) temperatures. The size for the optical image is of 7×7 μm, vertical spatial resolution 150 nm, spectral resolution is of up to 0.01 nm.

Nanoporous AOA membranes with a pore diameter of 10 nm and Si were utilized in the Raman spectroscopic studies.

2.2.4. Raman spectral analysis for monolayer graphene

Raman scattering of light is non-resonant scattering of light with the increase (Stokes line) or decrease (anti-Stokes line) of the frequency of the incident quantum of an electromagnetic field by the frequency of transition between the nearest levels [21, 29]. The most intensive Raman scattering occurs on free charge carriers (Compton effect). In our case, the anti-Stokes lines of Raman scattering are recorded with a decrease in the energy due to the transfer of an energy quantum to nuclear vibrational degrees of freedom in transitions between vibrational levels residing in electronic terms. The electron term is a potential-energy well of electron field where the nuclei oscillate. But electron-hole pairs residing in an impurity-free graphene plane annihilate in the valley $K(K')$. It signifies that C nuclei do not oscillate in the valleys $K(K')$. If graphene charge carriers are excited in a point Γ of the graphene

Brillouin zone then bound electron-hole pairs with the binding energy E_g equal to an energy gap in the Γ appear resulting in a breakdown of the $\pi(\mathrm{p}_z)$ shielding of a network of σ C−C bonds from the external electric fields. As results, high-frequency longitudinal nuclei vibrations along the network of σ C−C bonds stems from the partial shielding of the network. A Raman band which indicates the vibrational modes is called as the G band (see [30, 31] and references therein).

The Raman G band can be splitted in SWCNT Raman spectra into two pikes $G^{\pm}$ which correspond to vibrations along (G^{+}) and across (G^{-}) nanotube-axis direction.

By shifting the Fermi level, impurities in the graphene plane cause to prevail an electron density over hole one in the conduction band and, correspondingly, the electron term emerges in the Dirac point. A band of the Raman spectrum which indicates the longitudinal in-plane oscillations of nuclei in the valley is named as the defect peak D. For lack of the energy gap in the Dirac point a position of the D peaks changes over a much larger range than the G peak under an environment action shifting the Fermi level (see [32] and references therein).

From one side, since the graphene is related to genuine two-dimensional materials out-of-plane vibrational modes are forbidden. But, from another side, the conical graphene band structure is formed by three-dimensional (3D) Coulomb interactions between $\pi(\mathrm{p}_z)$ electrons which are out of the σ-bond network. A graphene-plane warp (curvature or torsion) facilitates escape of the C nuclei from the graphene monolayer owing to an action of centrifugal force and, correspondingly, stimulates the emerging transversal nuclei oscillations. A transversal low-frequency vibration produced by the curvature of the rolled graphene plane in the CNT is called as a radial breathing mode (RBM). Meanwhile the CNT diameter periodically increases. Let us to refer a transversal low-frequency vibration produced by the torsion to a bending mode (B mode).

Raman spectra of original CNT.

The recorded Raman spectra of the original carboxylated CNTs indicate the G and D bands near the Γ and Dirac points, respectively, and two RBMs (labeled as $\mathrm{RBM}_i, i = 1, 2$) and one B mode (see Fig. 1). The Raman spectral bands D and D' shown in Fig. 1b reveal the existence of defects in the graphene lattice and correspond to optical transverse and longitudinal in-plane vibrations in the vicinity of the point $K(K')$ [33]. The peak D'' indicates a longitudinal acoustic mode in the vicinity of the point $K(K')$ [33]. Also other at least four strong peaks are visible, and can be attributed, in order, to a intermediate frequency mode IFM^{-}, IFM^{+}, $2D$ (also called as G'), and $2G$ bands with doubled frequency of the G mode [31]. Let us list all observed frequencies of the CNT vibrations. They take the following values: 106.49 (B), 160.18 (RBM_1), 298.278 (RBM_2), 1096.49 (IFM^{-}), 1144.46 (IFM^{+}), 1333.72 (D), 1569.01 (G), 2441.72 ($D'' + D$), 2668.24 (G'), 2905.45 ($D' + D$), 3197.05 ($2G$) cm^{-1}.

2.2.5. Physicochemical characterization of carboxylated carbon nanotubes

Let us estimate the CNTs diameters using the formula [34]

$$\omega_{RBM} = \frac{227}{d_t}\sqrt{1 + C_{env} d_t^2} \qquad (2.1)$$

where C_{env} quantifies the environmental effect on the RBM frequency, d_t is a SWCNT diameter. We estimate approximately the C_{env} at zero in the case of the isolated original carboxylated few-walled CNTs. The CNT diameters are estimated at 1.48 and 0.761 nm for the RBMs of 160.18 (RBM_1) and 298.28 cm^{-1} (RBM_2), respectively. CNTs with such diameters are single-walled ones.

TEM images of the original carboxylated few-walled CNTs are presented in Fig. 3. Accordingly to the TEM image at 270,000× magnification, the CNTs form the horizontally-arranged fibers. The CNTs with the different diameters differ in their mechanical properties because the CNTs fibers can be rigid rods

or have the form of spirals and springs (see Fig. 3). Since the rigidness and elasticity are features inherent of semiconducting and metallic SWCNTs, respectively, the original CNT fibers consist of the rigid semiconducting or flexible (elastic) metallic CNTs.

In what follows we show that the inverse stearic-acid micelles with CNT inside contain SWCNTs of same type only (metallic or semiconducting).

CNT sorting.

The original hydrophilic CNTs being in a mixture of hexane with stearic acid are assembled into micelles. The CNTs inside the stearic acid micelles roll up into coils with a diameter of 0.1 μm as TEM- and SEM- images show. After dropping onto the hydrophilic surface of Si/SiO_2, the hydrophobic inverse micelles congregate together to minimize the contact with the hydrophilic support. According to Inset to Fig. 1b, in reflected light, dark micellar CNT conglomerates and bright rainbow micellar CNT associates are observed. Semiconductor crystals are transparent in the optical range, and, correspondingly, appear dark in reflected light. Contrary to this, the luster observed is typical for metals. Meanwhile, the bright rainbow micellar metallic-CNT associates surround more hydrophilic semiconducting CNT arrays on the outside. The micellar metallic-CNT associates prefer to adhere on the surface of the semiconducting CNT conglomerate, because the metallic micellar CNTs are less hydrophilic ones than the semiconducting ones. Raman spectra of the dark conglomerates and bright associates are typical Raman spectra of semiconducting and metallic SWCNTs, respectively (see Fig. 1b). The Raman torsional B mode is inherent in recording the Raman spectra of the elastic metallic SWCNTs only because semiconducting SWCNTs are rigid. The splitted G' band in the Raman spectrum of the metallic CNTs indicates vibrations near the Dirac points $K(K')$ of the spiral CNTs along (G'^{+}) and across (G'^{-}) helix, respectively. The characteristic frequencies for the micellar metallic CNTs are of 138.81 (B), 300.968 (RBM), 1364.77 (D), 2727.74 (G'^{-}, $2D^{-}$), 2747.81 (G'^{+}, $2D^{+}$), 3150.47 ($2G$) cm^{-1}. The characteristic frequencies for the Raman spectra of the micellar semiconducting CNTs are of 174.54 (RBM), 1345.91 (D), 1564.93 (G^{-}), 1592.2 (G^{+}), 1747.23 (M), 2001.43 (iTOLA), 2446.29 ($D'' + D$), 2680.37 ($2D$), 3186.08 ($2G^{+}$).

One concludes that higher frequency RBM (298.28 cm^{-1} in the Raman spectrum recording from the original CNTs) is related to the micellar metallic SWCNTs. The RBMs for the micellar CNT increase relative to their values for the original CNTs due to interactions between the nanotubes. The environmental coefficient C_{env} estimated by the formula (2.1) is equal to 0.0312 for the micellar metallic SWCNTs of 0.761-nm diameter. The large value of C_{env} equal to 0.0938 is a feature of the micellar semiconducting CNT. It signifies that the micellar semiconducting SWCNTs are very tightly packed inside the conglomerates. Using the following formula [22]:

$$d_t = \frac{0.246}{\pi}\sqrt{(n^2 + nm + m^2)} \qquad (2.2)$$

one gets the index $(n, m) = (7, 4)$ for the SWCNTs of the smaller radius. It is also a sign of the fact that they are of metal type because $\mathrm{mod}[(n - m), 3] = 0$.

After separating the original mix of different-type CNTs on the micellar semiconducting and metallic SWCNTs and then dropping the inverse micelles on the deionized-water surface the metallic SWCNTs form a Langmuir monolayer only as recorded Raman spectra of the bilayer of Fe(II)DTP-decorated CNT deposited on the Si support testify (see Fig. 2). The Raman metallic-SWCNT bands are exhibited among with the Raman bands of the Fe(II)DTP [17]. The environmental coefficient C_{env} for the CNT bilayer decreases relative to its value for the inverse micelles with the metallic SWCNTs from 0.0312 to 0.0303 due to the lack of interactions in the direction orthogonal to the CNT axis.

So, the only metallic SWCNTs remain at the subphase (water) air interface due to the fact that the semiconducting-SWCNT conglomerates

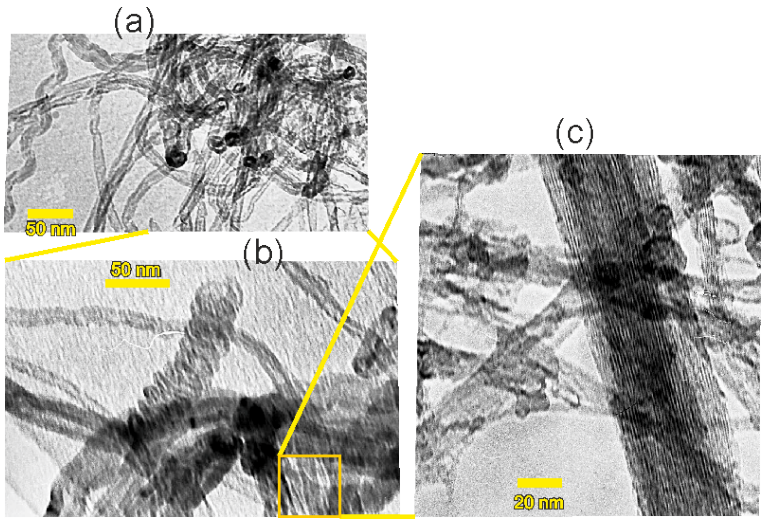

FIG. 3. TEM images of fibers of original carboxylated few-walled CNTs at 72,000× (a), 100,000× (b), and 270,000× (c) magnifications.

being denser and more hydrophilic and containing thicker and, correspondingly, more massive CNTs move into the subphase volume or sink, and the metallic micellar SWCNTs are retained on the subphase surface because of their amphiphilicity.

2.2.6. Simulation methods

To theoretically investigate the problem one use pseudo-Dirac and pseudo-Dirac-Weyl graphene hamiltonians.

The massless pseudo-Dirac fermion model of graphene presents itself a tight-binding graphene approximation near the Dirac point [23], and its Hamiltonian operator reads $\hat{H}_0 = v_F\vec{\sigma}\cdot\vec{k}$, where $\vec{\sigma} = \{\sigma_x, \sigma_y\}$ is a 2D vector of two Pauli matrixes, $\vec{k}$ is the 2D momentum. Then, a graphene quantum dot can be considered as a graphene in some confining potential $V(\vec{r})$. The Hamiltonian reads $\hat{H} = \hat{H}_0 + V(r)$ with a scalar potential incorporated as a diagonal matrix [1]

$$\hat{H} = \begin{pmatrix} V(\vec{r}) & \hat{p}_- \\ \hat{p}_+ & V(\vec{r}) \end{pmatrix} \tag{2.3}$$

with the operators $\hat{p}_\pm$ given by

$$\hat{p}_- = -i\frac{v_F}{\hbar}\frac{\partial}{\partial x} - \frac{\partial}{\partial y}, \quad \hat{p}_+ = -i\frac{v_F}{\hbar}\frac{\partial}{\partial x} + \frac{\partial}{\partial y}.$$

Now, let us examine circular quantum dot with the radial step potential

$$V(\vec{r}) = \begin{cases} 0, & \vec{r}\notin D \\ V_0, & \vec{r}\in D \end{cases} \tag{2.4}$$

where region D is a circle with a radius R. Due to the system's symmetry, for the eigenproblem $\hat{H}\mathbf{\Psi} = E\mathbf{\Psi}$, and the spinor function $\mathbf{\Psi}$ with components $\mathbf{\Psi} = (\Psi_1, \Psi_2)$, the separation of variables can be achieved in the polar coordinates (ρ, ϕ) introduced via ordinary relations $x = \rho\cos\phi$, $y = \rho\sin\phi$.

Then, introducing the dimensionless variables $\rho \to \rho/R, \epsilon = RE/v_F$ we have

$$\begin{aligned} (V(\rho)-\epsilon)\Psi_1(\rho,\phi) \\ = -ie^{-i\phi}\left(\frac{\partial\Psi_2(\rho,\phi)}{\partial\rho} - \frac{i}{\rho}\frac{\partial\Psi_2(\rho,\phi)}{\partial\phi}\right), \\ (V(\rho)-\epsilon)\Psi_2(\rho,\phi) \\ = -ie^{i\phi}\left(\frac{\partial\Psi_1(\rho,\phi)}{\partial\rho} + \frac{i}{\rho}\frac{\partial\Psi_1(\rho,\phi)}{\partial\phi}\right). \end{aligned} \tag{2.5}$$

Substituting the spinor function

$$\begin{pmatrix}\Psi_1\\ \Psi_2\end{pmatrix}=\begin{pmatrix}e^{\imath m\phi}\,\psi_1(\rho)\\ \imath\, e^{\imath(m+1)\phi}\,\psi_2(\rho)\end{pmatrix}, \tag{2.6}$$

making designation $\xi=\epsilon-V(\rho)$, and accounting that ξ is a constant but different one in two regions $\rho<1$ (inner region of the quantum dot) and $\rho>1$ (outer region), we obtain the following system of the radial equations:

$$\begin{aligned}\xi\psi_1(\rho)&=-\psi_2'(\rho)-\frac{(m+1)\psi_2(\rho)}{\rho},\\ \xi\psi_2(\rho)&=\psi_1'(\rho)-\frac{m\psi_1(\rho)}{\rho}.\end{aligned} \tag{2.7}$$

Then, expressing $\psi_1(\rho)$ from the first equation of the last system we get

$$\psi_1(\rho)=\frac{-r\psi_2'(\rho)-mb(r)-\psi_2(\rho)}{\xi r} \tag{2.8}$$

and substituting it into the second one, we get the second order equation for $\psi_2(\rho)$ in the form

$$\rho\left(\xi\rho\psi_2''(\rho)+\psi_2'(\rho)(\xi+\rho V_0\delta(R-\rho))\right)-\psi_2(\rho)\left(\xi\left(m^2+2m-\xi^2\rho^2+1\right)-(m+1)\rho V_0\delta(R-\rho)\right)=0 \tag{2.9}$$

where we have accounted that the derivative of the radial step potential ($V(\rho)=V_0\theta(R-\rho)$) discontinuing at $\rho=R$ is a δ-function. Let us examine a case of very small ρ: $\rho,R\to 0$. Let us find the limit of $\rho\delta(R-\rho)$ when tending R to zero. Using the expression $\delta(R-\rho)=\frac{1}{\pi}\int_0^\infty\exp[ip(R-\rho)]dp$ the limit is equal to zero due to that

$$\begin{aligned}&\lim_{R,R-\rho\to 0}\rho\delta(R-\rho)\\ &=\lim_{R,R-\rho\to 0}\frac{\rho}{\pi}\int_0^\infty[1+ip(R-\rho)]dp=0.\end{aligned}$$

The case of the very small GQD will be analyzed in Section 3 in detail.

The pseudo-Dirac-Weyl fermion Hamiltonian $\hat{H}_D$ is obtained within the quasirelativistic Dirac–Hartree–Fock self-consistent field approach (see [24, 25]). It is a high-energy $\vec{k}\cdot\vec{p}$-Hamiltonian in a q^4 approximation for the quasirelativistic quantum exchange. The approximation is the series expanded around the Dirac point $\vec{K}(\vec{K}')$ in powers of difference $\vec{q}=\vec{p}-\vec{K}$ between the quasiparticle momentum $\vec{p}$ and $\vec{K}(\vec{K}')$. The expansion on $q\equiv|\vec{q}|$ is produced up to the terms of $O(q^4)$ inclusively. The deviations of eigenvalues of $\hat{H}_D$ from the low-energy massless pseudo-Dirac fermion model are of the order of $|q|^4$. Contrary to the non-relativistic graphene model, energy levels of the quasirelativistic graphene model are Kramer's doublets. The Kramer's doublet represents itself two levels at which electrons are placed with the opposite signs of spin and in the absence of quantum exchange the levels are degenerated. The relativistic quantum exchange removes degeneration on spin outside the Dirac valley, violating the particle-hole symmetry so that the degeneration of Dirac point is lifted outside Dirac valley and six minibands emerge near the Dirac point. Due to the removal of the degeneracy of the Kramer's doublets, each miniband represents a Weyl node–antinode pair. Fig. 4a shows the band structure of the graphene model characterized by the Dirac touching in the $K(K')$ point and six Weyl node–antinode pairs. The pseudo-Dirac-Weyl

fermions are confined in the $p-n$ $(n-p)$ graphene junction by a pseudopotential which staircase-like approximation near the graphene valley, $K(K')$, for i-th graphene lattice site belonging to the junction is determined as [10]

$$V_{i,R_s}(\vec{r}) = \pm(2\pi)^2\epsilon_{R_s}(q_i)\Theta\left(\lambda_i - R\right)\Theta(a-r) \times \sum_{\sigma,\sigma'}|u|^2_{\sigma}(r)|u|^2_{\sigma'}(r), \tag{2.10}$$

where $\lambda_i = \frac{2\pi}{q_i}$, q_i is a momentum of the graphene charge carriers residing in the i-th lattice site.

3. Klein-scattering pseudo-Dirac fermions in electrostatically-confined graphene $p-n$ junctions

Let us assume that a radius of the circular $p{-}n$ $(n{-}p)$ graphene junction is very small. Then, since the potential V is step-like flat, expressing $\psi_2(\rho)$ from the second equation of (2.7) and substituting it into the first one, one gets the equation for $\psi_1(\rho)$:

$$\psi_1(\rho)\left(m^2-\xi^2\rho^2\right) - \rho\left(\rho\psi_1''(\rho)+\psi_1'(\rho)\right) = 0 \tag{3.1}$$

with the general solution given by the superposition of two Bessel functions [26]

$$\psi_1(\rho) = c_1 J_m(\xi\rho) + c_2 Y_m(\xi\rho). \tag{3.2}$$

The last can be substituted into the second equation of (2.7) and one gets for $\psi_2(\rho)$ that

$$\psi_2(\rho) = -c_1 J_{m+1}(\xi\rho) - c_2 Y_{m+1}(\xi\rho). \tag{3.3}$$

The solution for the radial system should be a finite one at $\rho = 0$, so one has to omit the second term in the right sides of (3.2) and (3.3) as the Bessel function Y_m is singular at zero. Outside the quantum dot ($\rho > 1$) one has to use both functions in the solution (3.3). A boundary condition for the problem is the continuity of the eigenfunctions at the GQD boundary ($\rho = 1$). An important point to the problem is that eigenfunctions can not belong to the bound states because asymptotically at infinity ($\rho \to \infty$) all Bessel functions trend to slowly damping plane waves $J_m(\xi\rho) \to \sqrt{\frac{2}{\pi\xi\rho}}\cos(\xi\rho - m\pi/2 - \pi/4)$, and the same formula for Y_m with the substitution of sin instead of cos.

3.1. Graphene charge carriers inside the potential well

Let us designate the coefficients c_1, c_2 in the solution (3.2)-(3.3) by additional upper indexes i and o for inside and outside region of the quantum dot, respectively. Matching solutions for both spinor components at $\rho = 1$ and choosing the normalization constant in the interior region with $c_1^i = 1$ (due to linearity of the equation one can choose arbitrary normalization) we get the following linear system to determine of the coefficients c_1^o, c_2^o:

$$J_m(V_0-\epsilon) = c_1^o J_m(\epsilon) + c_2^o Y_m(\epsilon), \tag{3.4}$$

$$-J_{m+1}(V_0-\epsilon) = c_1^o(-J_{m+1}(\epsilon)) - c_2^o Y_{m+1}(\epsilon). \tag{3.5}$$

The determinant d of the system of Eqs. (3.4) and (3.5) is given by the formula

$$d = J_{m+1}(\epsilon)Y_m(\epsilon) - J_m(\epsilon)Y_{m+1}(\epsilon). \tag{3.6}$$

Using the properties of the Bessel functions the last expression can be simplified into the following formula $d = \frac{2}{\pi\epsilon}$. Accordingly to the last formula, d does not depend on V_0 and m and is non-zero for all real values of energy ϵ. It signifies that the obtained real-valued solution of the eigenproblem is continuous in space as it is shown, for example, in Fig. 4b.

3.2. Scattering on a potential barrier

Let us use the Hankel functions of the first and second kind $H_m^{(k)}(z) = J_m(z) \pm \imath Y_m(z)$, $k = 1, 2$ for the outer region. Let us study the

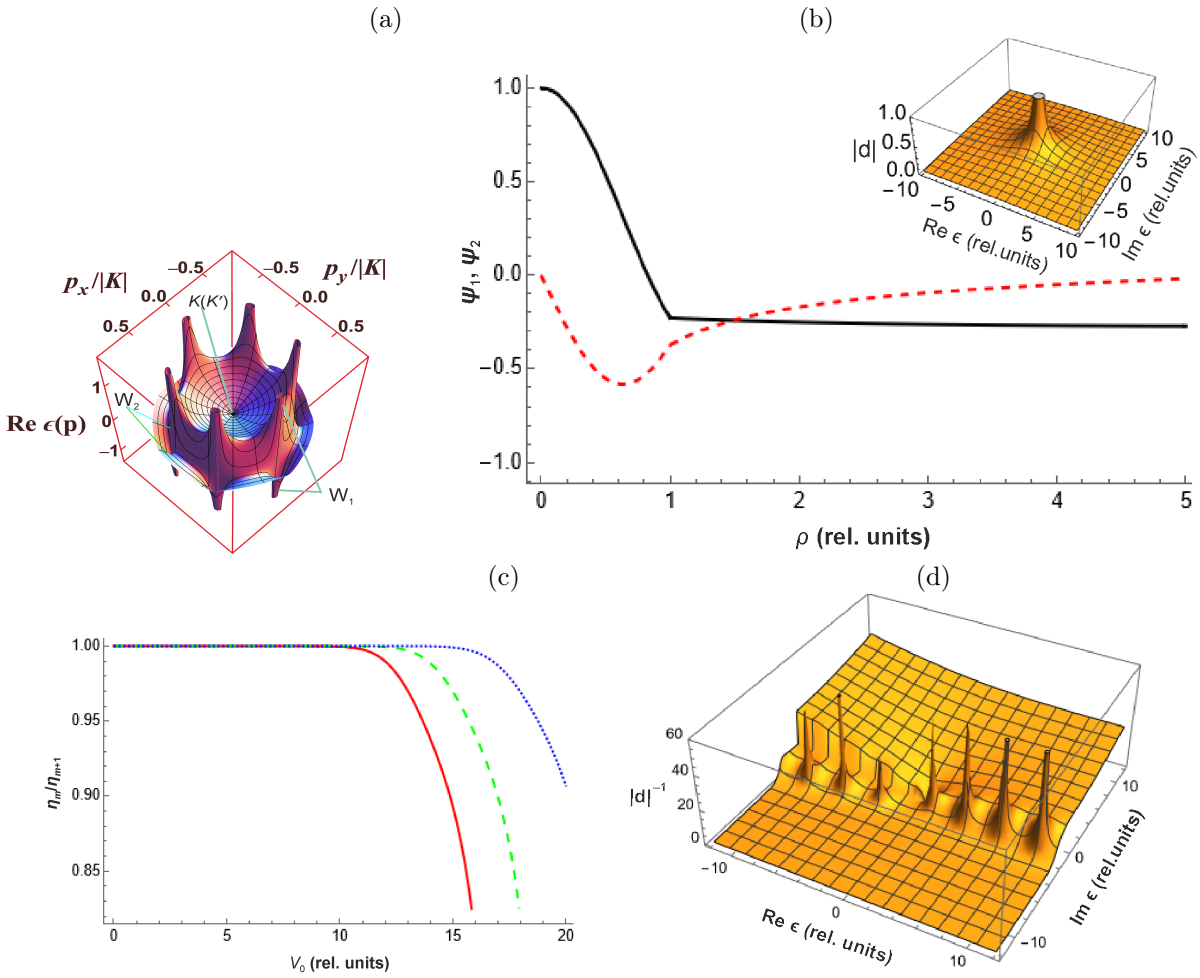

FIG. 4. (a) Splitting of Dirac cone into replicas for graphene in the Dirac–Hartree–Fock quasirelativistic approximation, q^4 approximation for the exchange interactions. Two W_1, W_2 of the six pairs of Weyl nodes–antinodes: two sources and two sinks and the Dirac valley $K(K')$ are indicated. (b) The upper (solid line, black) and lower (dashed line, red) components ψ_1 and ψ_2 of the spinor eigenfunction for the case of $m = 0$, $\epsilon = 0.09$, $V_0 = 3$. The determinant of the matching system is shown in Inset. (c) The dependence of the η_m/η_{m+1} upon the confining potential height for three values of m ($m = 15$ –red, $m = 17$ – green, $m = 20$ – blue). The region with approximate unity value of the ratio corresponds to the total reflection case. (d) The absolute value of the inverse determinant of the system (3.11) as a function of the complex energy ϵ for the case of $m = 0$, $V_0 = 20$.

consistency of linear equations describing the scattering on a potential barrier. For the radial scattering problem inside the GQD the solution consists of the transient wave and still is described by the Bessel J function with some amplitude $tJ_m(\xi r)$ (e.g., for the upper component), where t denotes a transmission coefficient. The solution outside the GQD is a superposition of two Hankel functions describing incident and scattered waves that is $H_m^{(1)}(\epsilon) + rH_m^{(2)}(\epsilon)$ again for the upper component (here r is a reflection coefficient). Then the matching system reads

$$\begin{aligned} tJ_m(V_0 - \epsilon) - rH_m^{(1)}(\epsilon) - H_m^{(2)}(\epsilon) = 0, \\ -tJ_{m+1}(V_0 - \epsilon) + rH_{m+1}^{(1)}(\epsilon) + H_{m+1}^{(2)}(\epsilon) = 0. \end{aligned} \tag{3.7}$$

The determinant of this system is

$$d = J_{m+1}(\epsilon - V_0)H_m^{(1)}(\epsilon) - J_m(\epsilon - V_0)H_{m+1}^{(1)}(\epsilon). \tag{3.8}$$

Now, let us to construct the system in the vicinity of the vanishing determinant. First, we do it for the energy values $\epsilon = V_0$ corresponding to the top of the potential well. In this case, the determinant of the matrix vanishes due to the properties of Bessel J functions at zero argument. Applying this energy value to the system, we get

$$-rH_m^{(1)}(V_0) - H_m^{(2)}(V_0) = 0, \tag{3.9}$$
$$rH_{m+1}^{(1)}(V_0) + H_{m+1}^{(2)}(V_0) = 0. \tag{3.10}$$

The last means that two equations are coinciding and the reflection coefficient can be expressed from the first equation as $r = H_m^{(1)}(V_0)/H_m^{(2)}(V_0)$. Taking into account the fact that the Hankel functions of the first and second kind at every given value of their argument are the conjugated complex numbers, the reflection coefficient as their ratio turns out to be unimodal. This corresponds to the same amplitude for the reflected wave with only a phase shift and therefore to zero value for the transmitted wave. We prove the last numerically. Let we designate $\eta_m = \arg\left(\frac{H_m^{(1)}(x)}{H_m^{(2)}(x)}\right)$. The simulation results are shown in Fig. 4c. As one can see, there exists a region of the potential height V_0 where for sufficiently high values of m the ratio η_k/η_{k+1} is equal to 1. This means that the linear dependence between the equations (3.9) and (3.10) exists for sufficiently small V_0 and sufficiently high m. The last is a total wave reflection case that hardly be considered as a bound state. Thus, the numerical results confirm our statement.

Now, let us prove that for any non-trivial complex root of the equation (3.8) the system for matching conditions (3.7) is inconsistent and has no solutions at all. With this in mind we normalize the system (3.7) in such a way to produce unit coefficients at variable t in every equation:

$$\begin{aligned} t - r\frac{H_m^{(1)}(\epsilon)}{J_m(V_0-\epsilon)} &= \frac{H_m^{(2)}(\epsilon)}{J_m(V_0-\epsilon)}, \\ t - r\frac{H_{m+1}^{(1)}(\epsilon)}{J_{m+1}(V_0-\epsilon)} &= \frac{H_{m+1}^{(2)}(\epsilon)}{J_{m+1}(V_0-\epsilon)}. \end{aligned} \tag{3.11}$$

For a given m, if complex energy ϵ is a complex root of the determinant of the system, the only way for the system to be consistent is the equality of the right hand sides of both equations (3.11):

$$\frac{H_m^{(2)}(\epsilon)}{J_m(V_0-\epsilon)} - \frac{H_{m+1}^{(2)}(\epsilon)}{J_{m+1}(V_0-\epsilon)} = 0. \tag{3.12}$$

Equating the determinant (3.8) to zero and expressing one of Bessel function, after its substitution into (3.12) we rewrite the left hand side of the expression (3.12) at vanishing determinant (3.8):

$$\frac{H_m^{(1)}(\epsilon)H_{m+1}^{(2)}(\epsilon) - H_{m+1}^{(1)}(\epsilon)H_m^{(2)}(\epsilon)}{H_{m+1}^{(1)}(\epsilon)J_m(V_0-\epsilon)} = \frac{\Delta}{H_{m+1}^{(1)}(\epsilon)J_m(V_0-\epsilon)}, \tag{3.13}$$

where the notation Δ has been introduced for numerator of (3.13). It is important to note that the height of the potential well is included in the denominator of (3.13) only and therefore does not influence on the validity in the condition (3.12) in physically reasonable region of complex plane ($|\epsilon| \sim O(V_0)$), so we can consider only the numerator Δ. Using properties of the Bessel functions, one can simplify it to the following

$$\Delta = \frac{4i}{\pi\epsilon}. \tag{3.14}$$

We arrive to contradiction with the condition (3.12). Thus, we have proved that for a non-trivial complex root of the equation (3.8) the system of matching conditions (3.7) is inconsistent and has no solutions at all.

To be less formal, let us present a numeric example. In Fig. 4d the inverse absolute value

of determinant (3.8) is shown as a function of the complex energy parameter ϵ. The zeroes of the determinant (3.8) are visible as pikes in the Fig. 4d. Numerically we find the first complex root $\epsilon = 3.95744 - 1.47721\imath$. After substitution of this value into the matching condition system (3.11) we obtain the following linear system with numeric coefficients

$$1.t - (1.01973 + 0.160047i)r = -0.0390394 + 0.0318167i, \quad (3.15)$$

$$1.t - (1.01973 + 0.160047i)r = 0.0409105 - 0.0408179i. \quad (3.16)$$

As one can see, indeed the determinant of the last system vanishes because the left hand sides of the system coincide. It signifies that a complex root of the (3.8) (which is called as "resonance condition" in paper [3]) exists really but the right hand sides are different for both equations of system (3.7). The last means that the system is inconsistent for the obtained complex root and there are no solutions at all in this case.

4. Emerging Klein resonances in single-walled carbon nanotubes

In this section one presents experimental evidence for Klein resonances excited by electron beam and light scattering in the arrays of single-walled carbon nanotubes. The crystal structure of the CNT LB-monolayers is exhibited through sharp facet pattern and edge abruptness for grains entering the CNT LB-film (see the AFM-image of the CNT bilayer in Fig. 5a, left). The splitted vibrational bands are observed in the Raman bilayer spectrum which characteristic frequencies are of 136.047 (B^-), 152.133 (B^+), 300.895 (RBM), 1371.02 (D), 2443.19 ($D'' + D$), 2747.14 (G'^-, $2D^-$), 2776.64 (G'^+, $2D^+$). The higher-frequency bending vibration (B^+) corresponds to nuclei oscillations in the monolayer plane, the lower frequency one (B^-) corresponds to the out-of-plane oscillations. The model of the bilayer structure is inset into the right upper corner of Fig. 2.

4.1. Microdiffraction and electron backscatter diffraction patterns of SWCNT LB-arrays

Fig. 5c shows a representative spherical Kikuchi map reconstructed from the experimentally collected electron backscatter diffraction patterns of the CNT bilayer. A distinct pattern of Kikuchi lines is exhibited on the electron backscatter diffraction pattern. The Kikuchi bands are approximately similar to a Kikuchi pattern of the hexagonal graphite for 7–8 bands, but not identical to it (higher mean angular deviation (MAD) is nor small enough, MAD ~ 1.078 and more). This indicates a structure locally similar to one of graphite 2H which rhombic unit cells are aligned transversely to the monolayer space.

The CNT bilayers and three-monolayer CNT LB-films would produce two related microdiffraction spots corresponding to the SWCNTs of opposite chirality (whose axes are in opposite directions) or the diffraction spots associated with a range of CNT chiral angles would form arcs. Arrangement of the microdiffraction reflections shown in Fig. 5d indicates only one diffraction spot for one monolayer of the CNT LB-films. It signifies that monodispersed crystals are formed from SWCNTs with one CNT chiral angle. The two primary directions indicated by the hexagonal microdiffraction patterns (see Fig. 5c) correspond to the so-called tube-radius reflection (R_t) of 0.512 nm and, orthogonal to this, a spacing of 0.236 nm corresponding to the spacing of the graphite hexagons (0.24 nm). For the arrangement of the monolayer-CNT ends on a rhombic lattice the tube-radius reflection equal to half a distance between nearest crystal planes passing through the centers of CNT cross-section is connected with the nearest-neighbor carbon-carbon distance (d_c) between atoms belonging to adjacent tubes by a following formula:

$$R_t = \frac{1}{2}(d_t + d_c)\cos(\pi/3) \quad (4.1)$$

where $\pi/3$ is the angle in the unit cell of the

rhombic lattice. Using the formula (4.1) for the metallic SWCNTs of 0.761-nm diameter one gets that d_c is equal to 0.42 nm. For comparison, the distance between the nearest carbon atomic layers in graphite is of 0.34 nm less than for the CNT end arrays due to stretching CNT bodies.

The 3D background of the interactions between the graphene charge carriers and the electron beam originates the SWCNT-image thickening. The apparent thick-CNT-fiber diameter of 22.8 nm is 2.5 times larger than the size of ellipsoidal cross-section of 9.1 nm. A visual increase in the true CNT-fiber diameter occurs due to the dark regions adjacent to the central light region of the CNT LB-fiber image. The small-diameter CNT-fibers and individual SWCNTs look like the thick CNT fiber (see fig. 5b).

Thus, thickness of the TEM image of the SWCNT deposited on the support increases by 2.5 times compared to free nanotube diameter determined from the CNT elliptic cross-section. Such an increase in diameter of CNT is also observed in a scanning tunnelling microscope [27]. One concludes that the proper CNT diameter being 2.5 times less than the apparent CNT diameter (1.9 nm) is of 0.76 nm in accordance with the Raman spectroscopic data. In the dark regions where the electron beam scatters most strongly, the electrons move tangentially along the CNT-fiber or the single CNT, but the electrons do not bend around the carbon atoms because the electron wavelength is very small (0.037 Å). At the tangent point, the projection of the electron momentum and, correspondingly, the momentum transferred to the graphene plane of the individual CNT or peripheral CNTs in the fibers, is maximal.

The CNT bilayer deposited on the cleavage of nanoporous AOA which was coated by 5-monolayer Fe(II)DTP film is suspended into the pores and, correspondingly, an interaction between the bilayer and support falls down (see Fig. 5a, right). The CNT bilayer is almost transparent in the regions of transversal electron beam incidence. The lack of interactions between the electron beam and graphene charge carriers indicates Klein tunnelling through the crystalline CNT monolayers.

In the TEM-image, the CNT monolayers appear as dark areas in the pores labeled by "3" and "4" (see Fig. 5a, right). The thickness (3.9 nm) of the bilayer which is located in the pores "3" and "4" is equal to twice the apparent CNT diameter (1.9 nm) with the added distance between the hydrophilic surfaces of the CNT monolayers (1.0 nm). The TEM-images of the CNT bilayer are darkened where the beam is tangent to the surface of the CNT LB film (see Fig. 5a, right). It signifies that the Klein resonances are created in the CNT film as in a genuine 2D material. The electron beam directed parallel to the CNT-monolayer surface, propagates freely between the two CNT LB-monolayers and is scattered uniformly in the monolayer bulk the thickness of which equals to the apparent CNT diameter (1.9 nm). It once again confirms that the proper CNT diameter being 2.5 times less than the apparent CNT diameter is of 0.76 nm in accordance with the Raman spectroscopic data.

So, the radiation defects are activated along the whole surface of the all CNTs entering the dark region due to the 2D translational symmetry, but not because of the CNT curvature.

5. Comparison between theoretical predictions and experimental data

Experimental evidence presented in Experimental Section 4 indicates the following features of the Klein resonances in the rolled graphene monolayer. When scattered by carbon atoms, the graphene carriers excited into the conduction band from the valence band do not evanesce, on the contrary, their energy and momentum are returned to the normally incident electron beam after electron-hole annihilation due to the Klein tunneling. Therefore, the central regions of the CNT fiber and individual CNTs on

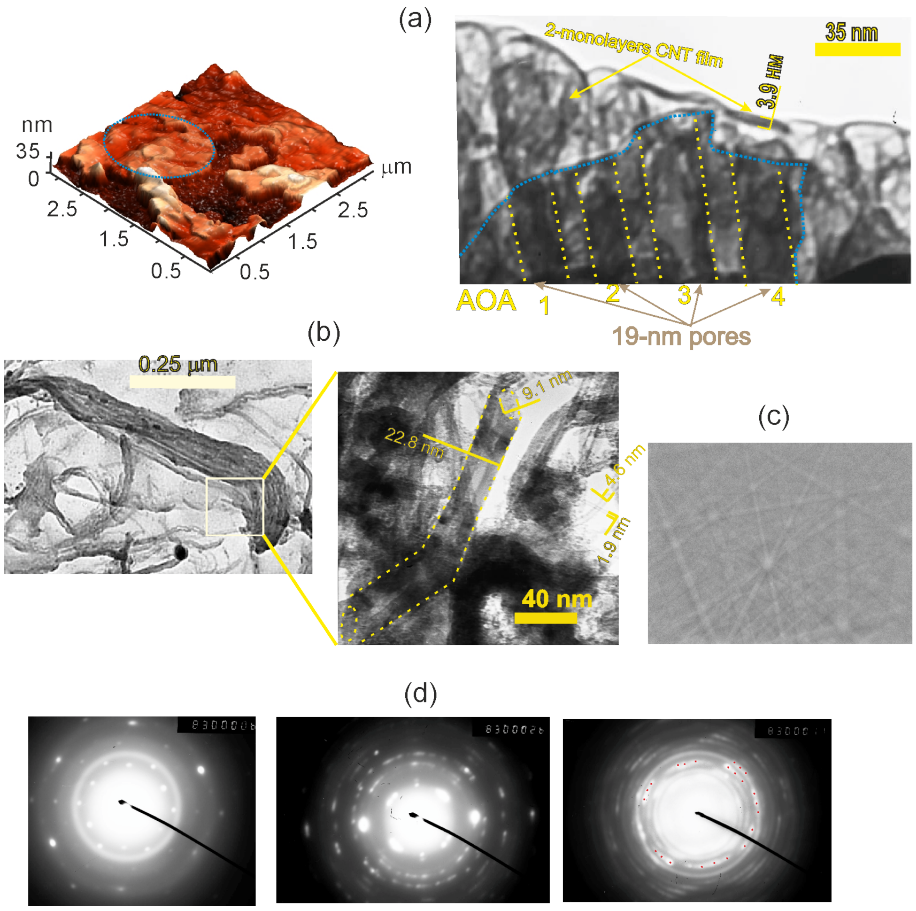

FIG. 5. AFM (a, left) and TEM -images (a, right; b) and/or representative electron backscatter-diffraction (c) and mictodiffraction patterns (d) of 2-,3-х монослойных CNT LB-films. The magnifications are 140,000 (a, right), 19,000 (b, left), and 190,000 (b, right) times the original size. The CNT bilayers are arranged on the supports: a graphite fresh cleavage (a, left), fresh cleavage of AOA with pore diameter of 19-nm (a, right), grids (b, d) and SiO_2 2.8-μm thick (c); the supports were previously covered by six (a, left), or five (a, right; c; d, left and middle), or three (b) Fe(II)DTP monolayers. The 3-monolayer CNT film was deposited on the cooper grid without the Fe(II)DTP covering. A large crystal grain shown in the figure (a, left) is encircled by a blue oval, a blue curved line is drawn along the CNT-bilayer edge imaged on the picture (a, right); and the elliptic 9.1-nm cross-sections of the thick CNT fiber are drawn by yellow ovals to improve perception. The images of the thick and thin CNT fibers with the apparent diameters of 22.8 and 4.6 nm, respectively and image of CNT with the apparent diameter of 1.9 nm are denoted by yellow lines along an interface between the CNTs and their environment. The dashed yellow lines provides a guide to the eye for the 19-nm AOA pores.

the TEM-images are light (see Fig. 5b). In the regions where the electron beam is tangent to the CNT wall, one observes the Klein resonances propagating freely due to the translation symmetry. Due to the curved CNT surface, the Klein resonances would constructively interfere and behave like whispering-gallery modes. If this type of Klein resonance is a long-lived one, then the energy and momentum would be pumped out of the electron beam, and, correspondingly, a darkening of the CNT-image would occur at that location. But, since the CNT-interior image is light the graphene charge carriers obliqued by the incident electron beam in the direction

orthogonal to the CNT axis do not constructively interfere. This experimental fact validates the theoretical predictions from Section 3 that the whispering-gallery modes around CNT do not appear because the geometrical curvature is unable to break the electron-hole symmetry of chiral massless graphene charge carriers. In the theoretical section 3 one has proved that the existence of Klein resonances is impossible in the case of pseudo-Dirac fermions because of the chirality conservation law.

However, near the Dirac point within the pseudo-Dirac-Weyl fermion model GQD the graphene charge carriers are confined by the staircase-type potential that is determined in each i-th graphene lattice site belonging to the junction by the radial step potential (2.10). It signifies that the Zak curvature and centrifugal force compete with each other in the following manner. Let a graphene charge carrier with an energy E be in a state of total reflection for the i-th radial step potential well. The charge carrier is totally reflected due to the action of the centrifugal force and, as a result, it falls into the $(i+1)$-th radial step potential well. To satisfy a law of energy conservation the charge carrier has to reside near a bottom of the $(i+1)$-th well for some time Δt that its energy variation ΔE satisfies a Heisenberg–Bohr's uncertainty principle ($\Delta E \Delta t \geq \hbar$). Then, the Zak curvature reduces energy levels from $E+\Delta E$ to E (without violating the law of conservation of energy) and, correspondingly, the graphene charge carrier comes back to the total reflection state of i-th well, and so on. In this sense, the total reflection states of the pseudo-Dirac-Weyl hamiltonian are stable.

Collisions between the electron beam and graphene lead to the appearance of vacancies and free electrons. The electron-hole pairs due to very short lifetime (~ 0.3 ps) [28] destroy, having not enough time to interact with the radiation defects. However, the radiation vacancies can be occupied by the long-lived negatively charged Klein resonances. Meanwhile, free electrons would be held by the positively charged Klein resonances. The darkened peripheral regions of the CNT TEM-images in Fig. 5b testify that there are the pairs of the topologically-nontrivial spatially separated positively and negatively charged Klein resonances. Such a confinement is possible for electron density vortices in the graphene unit cell due to the topological nontriviality of the vortex modes. These topologically nontrivial charge carriers reside in the Dirac-Weyl fermion graphene model as cores of the vortices. Since the topological charge conservation law forbids the graphene charge carriers to annihilate with the vacancies and free electrons, no energy and momentum leakage back into the graphene plane happens.

Thus, the existence of the dark regions in the CNT TEM-images is a signature of the non-Abelian statistics of graphene charge carriers. As a result, the central regions of the fibers and individual CNTs are free of delocalized charge carriers, and the electron beam touching to the CNT wall is scattered creating the dark peripheral regions in the fibers and individual-CNT images.

A high-energy electron touching with the surface of the LB-monolayer, transfers a momentum to the graphene plane that the Klein resonances discussed in Section 4 are formed. Since the magnitude of this momentum is sufficient to excite the monolayer pseudo-Dirac electrons and holes into the flat regions of the Dirac-Weyl band structure, the non-trivial topology of the graphene charge carriers is revealed through the darkening observed, but not because of the CNT curvature in agreement with the theoretically predicted absence of Klein resonances in the pseudo-Dirac fermion graphene model. Meanwhile, the vortical (antivortical) modes are deconfined that the superpositions of the vortical (antivortical) modes are the pseudo-Dirac electrons (holes). The proliferating vortexes hold the very large energy of the incident electron and are very massively due to the zero Fermi velocity in the flat bands. Contrary to this, the electron beam orthogonally incident on the graphene plane weakly interacts with it due to the Klein tunnelling.

High intensity of the Raman bands of Fe(II)DTP entering the Raman spectrum for the CNT bilayer indicates an electron-hole pair production in the graphene planes when exposing to the laser radiation (see Fig. 2). A huge number of the free graphene charge carriers, oscillating in resonance with the vibrations of the molecular Fe(II)DTP groups, reproduces their Raman spectra shown in Fig. 2. Since the crystalline decorated metallic-CNT monolayers suspended in the 10-nm pores of AOA are not doped for lack of an interaction between the CNTs and support, no pseudo-Dirac fermions occupy the Fermi level being in the Dirac touchings of the graphene band structure and, correspondingly, the characteristic graphene Raman bands does not appear in the CNT-bilayer Raman spectrum. It signifies that the proliferation of vortical-antivortical modes similar to the nodes in the warping regions of the Dirac-Weyl graphene hamiltonian happens.

As a result, the topologically-nontrivial 2D-defects activated by the electron beam and laser radiation are hosted at the CNT LB-monolayer.

6. Conclusion

So, all states of the pseudo-Dirac fermion model GQD are unstable due to that the "resonance condition" to construct "quasi-bound" states for the pseudo-Dirac fermion GQD with a finite life time, leads to the inconsistent system of linear equations describing matching conditions for the solution inside and outside the GQD. The so-called "strong localized state" of an electron in the quantum dot [1] in fact is a state of total reflection (with a given m) of an electron on a graphene quantum dot for very specific case of the electron energy. Therefore the pseudo-Dirac fermion hamiltonian can not be used as valid to simulate any Klein-tunnelling applications.

Based on the experimental data on electron and light scattering an idea of topological stability for the Klein resonances within a quasi-relativistic graphene model with pseudo-Dirac-Weyl hamiltonian is developed. The theoretical predictions are in a good agreement with the experimental data.

The advantage of Klein tunneling tuning by our method based on graphene models with topologically-nontrivial Brillouin zone is in possibility to realize electrostatically confined graphene $p-n$ $(n-p)$ junctions which states are stable.

References

[1] P. Hewageegana, V. Apalkov. Electron localization in graphene quantum dots. Phys. Rev. **B 77**, 245426 (2008).

[2] P. Hewageegana, V. Apalkov. Trapping of an electron in coupled quantum dots in graphene. Phys. Rev. **B 79**, 115418 (2009).

[3] Ch. Gutiérrez, L. Brown, Ch.-J. Kim, J. Park, A.N. Pasupathy. Klein tunnelling and electront rapping in nanometre-scale graphene quantum dots. Nature Physics. **12**, 1069 (2016).

[4] Zh.-Q. Fu, K.-K. Bai, Ya-N. Ren, J.-J. Zhou, L. He. Breaking whispering-gallery modes of massless Dirac fermions in graphene quantum dots by Coulomb interaction Phys. Rev. **B 101**, 235310 (2020).

[5] A. Hansen, F. Ravndal. Klein's paradox and its resolution. Physica Scripta. **23**, 1033 (1981).

[6] Yu. Pan, H. Ji, X.-Q. Li, H. Liu. Quasi-bound states in an nanometer-scale graphene quantum dot under a magnetic field. Scientific Reports. **10**, 20426 (2020).

[7] Y.B. Zeldovic, V.S. Popov. Electronic Structure of Superheavy Atoms. Sov. Phys. Usp. **14**, 673 (1972).

[8] T.H. Boyer. Unfamiliar trajectories for a relativistic particle in a Kepler or Coulomb potential. American J. Phys. **72**, 992 (2004).

[9] Yu. Zhao, J. Wyrick, F.D. Natterer, J.R. Nieva, C. Lewandowski, K. Watanabe, T. Taniguchi, L. Levitov, N.B. Zhitenev, J.A. Stroscio. Creating and probing electron whispering gallery modes in graphene. Science. **348**, 672 (2015).

[10] H. V. Grushevskaya, G. G. Krylov, S. P. Kruchinin, B. Vlahovic, and Stefano Bellucci Electronic properties and quasi-zero-energy states of graphene quantum dots Phys. Rev. B **103**, 235102 (2021).

[11] Zh. Ge, Fr. Joucken, E. Quezada, D.R. da Costa, J. Davenport, B. Giraldo, T. Taniguchi, K. Watanabe, N.P. Kobayashi, T. Low, Ja. Velasco Jr. Visualization and Manipulation of Bilayer Graphene Quantum Dots with Broken Rotational Symmetry and Nontrivial Topology. Nano Lett. **20**, 8682 (2020).

[12] J. Lee, D. Wong, J. Velasco Jr, J.F. Rodriguez-Nieva, S. Kahn, H.-Z. Tsai, T. Taniguchi, K. Watanabe, A. Zettl, F. Wang, L.S. Levitov, M.F. Crommie. Imaging electrostatically confined Dirac fermions in graphene quantum dots. Nature Physics. **12**, 1032 (2016).

[13] Z. Hou, Y.-F. Zhou, X. Xie, Q.-F. Sun. Berry phase induced valley level crossing in bilayer graphene quantum dots. Phys. Rev. B. **99**, 125422 (2019).

[14] A. Matulis and F. M. Peeters, Quasibound states of quantum dots in single and bilayer graphene Phys. Rev. **B 77**, 115423(2008).

[15] P. Recher and J. Nilsson, G. Burkard, B. Trauzettel Bound states and magnetic field induced valley splitting in gate-tunable graphene quantum dots Phys. Rev. **B 79**, 085407(2009).

[16] E. Rossi, J. H. Bardarson, P. W. Brouwer, and S. Das Sarma Signatures of Klein tunneling in disordered graphene p-n-p junctions Phys. Rev. **B 81**, 121408R (2008).

[17] H.V. Grushevskaya, N.G. Krylova, I.V. Lipnevich, T.I. Orekhovskaja, B.G. Shulitski. Electrochemical nanobiosensor for real-time detection of gap junction-mediated intercellular communication activity. Adv. Mat. Lett. **8**(4), 531 (2017).

[18] H.V. Grushevskaya, N.G. Krylova, I.V. Lipnevich, T.I. Orekhovskaja, V.P. Egorova, B.G. Shulitski. Enhancement of Raman light scattering in dye-labeled cell membrane on metal-containing conducting polymer film. Int. J. Modern Phys. B. **30**, 1642018 (2016).

[19] Ch. Zhu, K. Kaufmann, K. Vecchio. Automated Reconstruction of Spherical Kikuchi Maps. Microscopy and Microanalysis. **25**, 912 (2019).

[20] V.A. Fock. *Fundamentals of Quantum Mechanics*. (Mir Publishing, Moscow, 1978).

[21] M. Walter, M. Walter. Ab Initio Wavelength-Dependent Raman Spectra: Placzek Approximation and Beyond. J. Chem. Theory Comput. **16**, 576 (2020).

[22] V.Sh. Gangoli, Ju. Azhang, T.T. Willett, S.A. Gelwick, E.H. Haroz, Ju. Kono, R.H. Hauge, M.S. Wong. Using nonionic surfactants for production of semiconductor-type carbon nanotubes by gel-based affinity chromatography. Nanomater. Nanotechnol. **4**, 19 (2014).

[23] A.H. Castro Neto, F. Guinea, N.M.R. Peres, K.S. Novoselov, A.K.Geim. The electronic properties of graphene. Rev. Mod. Phys. **81**, 109 (2009).

[24] H.V. Grushevskaya, G. Krylov. Quantum Field Theory of Graphene with Dynamical Partial symmetry breaking. J. Mod. Phys. **5**, 984 (2014).

[25] H. V. Grushevskaya, G. Krylov. Semimetals with Fermi velocity affected by exchange interactions: two dimensional Majorana charge carriers. Int. J. Nonlin. Phen. in Compl. Sys. **18**, 266 (2015).

[26] *Handbook of Mathematical Functions*. Eds. M. Abramowitz, I.A. Stegun. (Dover, New York, 1965).

[27] I.I. Bobrinetskiĭ, V.K. Nevolin, V.I. Petrik, A.A. Stroganov, Yu.A. Chaplygin. The atomic structure of nanotubes synthesized from a carbon mix of high reaction ability. Technical Physics Lett. **29** 347-349 (2003).

[28] J. Yang, Yu. Liu, H. Ci, F. Zhang, J. Yin, B. Guan, H. Peng, Zh. Liu. High-performance 3D vertically oriented graphene photodetector using a floating indium tin oxide channel. Sensors. **22**, 959 (2022).

[29] V.A. Fock. *Fundamentals of Quantum Mechanics*. (Mir Publishing, Moscow, 1978).

[30] D.R. Cooper, B.D'Anjou, N. Ghattamaneni, B. Harack, M. Hilke, A. Horth, N. Majlis, M. Massicotte, L. Vandsburger, E. Whiteway, V. Yu. Experimental review of graphene. ISRN Condensed Matter Physics. **56**, 2012 (2012).

[31] A. Jorio, R. Saito. Raman spectroscopy for carbon nanotube applications. J. Appl. Phys. **129**, 021102 (2021).

[32] H.V. Grushevskaya, A.I. Timoshchenko, E.A. Avdanina, I.V. Lipnevich. Clustering Artificial Atoms Induced by High-Frequency

Electromagnetic Radiation in Graphene Monolayers of Multiwalled Carbon Nanotubes. Int. J. Nonlinear Phenom. in Complex Syst. **23**,342 (2020).

[33] A.S. Egorov, V.P. Egorova, H.V. Grushevskaya, N.G. Krylova, I.V. Lipnevich, T.I. Orekhovskaya, B.G. Shulitsky. CNT-enhanced Raman spectroscopy and its application: DNA detection and cell visualization. Lett. in Applied NanoBioScience. **5**, 346 (2016).

[34] T.Araujo, P.B.C. Pesce, M.S. Dresselhaus, K. Sato, R. Saito, A. Jorio. Resonance Raman spectroscopy of the radial breathing modes in carbon nanotubes. Physica. E **42**, 1251-1261 (2010).